Inorganic Chemistry

pubs.acs.org/IC Article

Precursor Engineering for the Synthesis of Mixed Anionic Metal (Cu, Mn) Chalcogenide Nanomaterials via Solvent-Less Synthesis

Temidayo Oyetunde,* Siphamandla Masikane, Malik Dilshad Khan, Matthew P. Akerman, Helmar Görls, Neerish Revaprasadu,* and Winfried Plass

Cite This: *Inorg. Chem.* 2022, 61, 6612–6623 Read Online

ACCESS | Metrics & More | Article Recommendations | Supporting Information

ABSTRACT: Metal−organic ligands with mixed chalcogenides are potential compounds for the preparation of mixed anionic metal chalcogenide alloys. However, only a few of such ligands are known, and their complexes are not well explored. We have prepared homo- and hetero-dichalcogenoimidodiphosphinate $[(EE'P^iPr_2NH)]$ (E, E′ = Se, Se; S, S; S, Se) complexes of manganese and copper through metathetical reactions. The X-ray single crystal structure of $[Mn\{(SeP^iPr_2)_2N\}_2]$ **1** revealed a triclinic crystal system, with a $MnSe_4$ core unit, whereas the crystal structure determination of $[Mn\{(SP^iPr_2)(SeP^iPr_2)N\}_2]$ **2** indicated a triclinic crystal system with a $Mn(S/Se)_2$ unit. Both metal centers are tetrahedral, with two deprotonated bidentate ligands forming the coordination sphere. The free ligand was found to exhibit a gauche configuration in the solid state. The energies of the various rotamers of dithio-analogue were studied by DFT calculations. The decomposition behavior of complexes with homo- and heterochalcogenides was investigated, and the complexes were employed as single-source precursors to generate manganese and copper chalcogenides through solvent-less melt reactions between 500 and 550 °C. The deposited powders were characterized by powder X-ray diffraction (*p*-XRD), scanning electron microscopy (SEM), energy dispersive analysis of X-ray (EDAX), transmission electron microscopy (TEM), and elemental mapping. MnS, $MnSe_2$, and MnSSe phases were obtained from the decomposition of respective manganese complexes. In contrast, the decomposition of copper-based complexes yielded $Cu_{2-x}Se$ and the sulfur-doped Cu_3Se_2 phase from seleno- and mixed thio/seleno-complexes of Cu, respectively. The morphology ranged from random sheet-like structures to agglomerated platelets, while the selected area electron diffraction (SAED) revealed the crystalline nature of the materials. Depending on the nature of the complex and the temperature, different amounts of phosphorus were present as an impurity in the synthesized products.

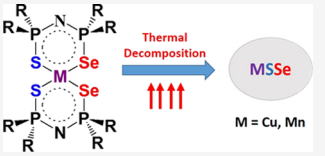

INTRODUCTION

Transition metal chalcogenides (TMCs) have emerged as potential materials for various important applications, such as solar cells, sensors, field-effect transistors (FETs), water splitting, photocatalysis, photovoltaics, supercapacitors, fuel cells, and thermoelectric materials.[1−10] In addition to binary metal chalcogenides, the mixed anionic solid solutions or alloyed compounds (e.g., $CdS_{1-x}Se_x$, $PbS_{1-x}Se_x$, $SnS_{1-x}Se_x$, and $Sb2(S_{1-x}Se_x)_3$) are of interest as, besides size and morphology, the properties of such compounds are also composition-dependent.[11−13] Moreover, aside from the flexibility of tuning the properties based on composition, the performance of such alloyed compounds is usually enhanced because of the synergistic effects from mixed anions.[13] The chalcogenide atoms have similar oxidation states and comparable electronegativity, and the formation of such mixed anionic inorganic compounds is favored when the parent binary metal chalcogenides exist in a similar crystal structure.[14] The synthesis of mixed anionic alloys is challenging because of the limited availability of suitable chalcogenide sources. Moreover, the difference in the precursor nature/reactivity may lead to the formation of secondary phases or undesired impurities. Therefore, the synthesis of mixed anionic metal chalcogenides requires the use of carefully designed precursors with comparable reactivity.

The use of metal−organic precursors (MOPs) often yields compounds with better control over stoichiometry and phase purity.[15] The MOPs are usually stable, can be stored for a long duration and, under specified reaction conditions, are advantageous for obtaining products with great reproducibility. Moreover, they are equally suitable for the fabrication of thin films and nanomaterials using different techniques.[16] Sulfur-based MOPs are relatively well explored as compared to their higher congeners, that is, selenium and tellurium. Commonly used MOPs for metal sulfides are xanthates, dithiocarbamates, thiourea, thiolates, thioethers, and thiosemicarbazone.[17] Selenium and tellurium-based MOPs are not well explored because of difficulties associated with their synthesis, limited choice of reagents, toxicity, and comparatively lower stability. For example, frequently used xanthates and dithiocarbamates

Received: February 15, 2022
Published: April 18, 2022

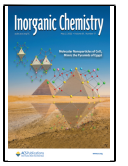

https://doi.org/10.1021/acs.inorgchem.2c00460
Inorg. Chem. 2022, 61, 6612−6623

are prepared by reacting alcohol or amine with carbon disulfide (CS_2) in the presence of a base. However, the selenium analogue of CS_2, that is, CSe_2 is highly unstable, obnoxiously smelling, and much more toxic than CS_2. On the other hand, tellurium preferably forms dialkylmonotelluride (R_2Te) or dialkylditelluride (R_2Te_2) rather than carbon ditelluride (CTe_2).

Dichalcogenoimidodiphosphinate ligands [$(EE'P_2R_4NH)$] (E, E′ = S, S; Se, Se; S, Se; Te, Te; R = ^{i}Pr, Ph) are bidentate ligands that exhibit an excellent coordination ability toward transition metals to form diverse cyclic inorganic complexes.[18−22] The ligand consists of a PNP backbone, two organic groups, and both phosphorus atoms are bonded to chalcogenide atoms, which can coordinate with the metal atom to form cyclic inorganic complexes. The interesting aspect of these ligands is that they can be engineered to contain either similar chalcogenide atoms (i.e., E = E′ = S, Se, Te) or different chalcogenide atoms can be selectively introduced (i.e., E, E′ = S, Se; S, Te; Se, Te). Sulfur and selenium are easily oxidized, and they react with the P^{II}/P^{III} system of $HN(PR_2)_2$ to generate $HN(PR_2E)_2$ ligands readily. However, unlike S and Se, tellurium is a metalloid and does not oxidize easily. Because of its large size and low tendency to oxidize, the Te-based ligand can be obtained by forming an alkali metal (Li/Na) salt through an in situ deprotonation.[63]

Recent developments on the synthesis of various nanostructured materials and nanocomposites (e.g., ternary systems, metal oxides, and metal selenides) have occurred through different techniques. These include sonochemical reactions,[25−27] thermal treatment/decomposition,[28,29] hydrothermal synthesis,[30,31] co-precipitation[32] combination of different techniques,[33] and calcination.[34] As the solid-state decomposition of MOPs results in the formation of metal chalcogenides, a mixed anion metal complex is expected to yield mixed metal chalcogenide alloys. The solid-state decomposition involves the solvent-less decomposition of an MOP under an inert atmosphere.[23] Different single-source precursors have been used to synthesize metal chalcogenide nanomaterials via solvent-less decomposition.[22] As compared to other techniques, the solvent-less decomposition method is scalable and economical with environmental benefits.[23,24] In addition, there are no negative or undesirable effects of solvents/surfactants in solvent-less synthesis.

Among the different inorganic materials, copper and manganese chalcogenides are of interest because of their wider availability, low toxicity, cost-effectiveness, and applications in diverse fields. Manganese chalcogenides exist in three different crystallographic phases, α-(rock salt), β-(zinc blende), and γ-(wurtzite), among which the α-phase is the most stable.[35−40] Likewise, copper chalcogenides exist in various stoichiometric ratios, ranging from metal-rich (i.e., Cu_2S and Cu_2Se) to stoichiometric compounds (i.e., CuS and CuSe),[41−43] while its crystallographic forms are orthorhombic, hexagonal, monoclinic, cubic, and tetragonal.[41,44] The multiple crystallographic modifications of these materials make it challenging to produce single-phase selectively with high purity. Moreover, obtaining a uniform size and morphology is also a challenge as it shows a range of morphologies such as spherical, sheet-like, discotic, hexagonal, or multifaceted polyhedral nanoparticles. The synthesis of sulfides of these metals (Cu, Mn), via MOPs, is well investigated, while the synthesis of their selenide-based compounds via MOPs is not adequately developed.

To the best of our knowledge, there is no report on the use of dichalcogenoimidodiphosphinate complexes to synthesize either manganese or copper chalcogenides. Herein, we report the synthesis of homo- and hetero-dichalcogenoimidodiphosphinate complexes of Cu and Mn. The mixed anion complexes were prepared in anticipation that the existence of their sulfide and selenide phases in similar crystallographic phases may favor the formation of mixed thio/seleno-alloys upon decomposition of the precursors. The crystal structures of manganese complexes were elucidated, and their thermal behavior investigated. The complexes were used to deposit metal chalcogenides through solvent-less melt reactions at 500 and 550 °C. The residual powder obtained was characterized by powder X-ray diffraction (*p*-XRD), scanning electron microscopy (SEM), energy dispersive analysis of X-ray (EDAX), transmission electron microscopy (TEM), and elemental mapping.

EXPERIMENTAL SECTION

Materials. Using a standard double-manifold Schlenk line connected to a vacuum pump, all synthetic procedures occurred under a dry inert atmosphere of nitrogen. The following chemicals were purchased from Sigma-Aldrich: chlorodiisopropylphosphine (96%) (toxic, handled with care in a well-ventilated area), 1,1,1,3,3,3-hexamethyldisilazane (99%) (toxic, handled with care in a well-ventilated area), anhydrous $MnCl_2$ (≥99%), and anhydrous $CuCl_2$ (≥99.95%), while selenium pellets, sulfur flakes, and powdered NaOMe were obtained from Fluka, Riedel-de Haën Honeywell, and ABCR, respectively. They were used without any alteration(s). All solvents were dried and obtained either through distillation or through molecular sieve storage.

Synthesis of Ligands. *Synthesis of [^{i}Pr$_2$P(Se)NHP(Se)^{i}Pr$_2$].* The synthesis of the ligand was performed according to the previous report.[45] Briefly, chlorodiisopropylphosphine (25 g, 26 mL, 164 mmol) in toluene (30 mL) was added slowly into a solution of hot toluene (50 mL) containing 1,1,1,3,3,3-hexamethyldisilazane (13.2 g, 17 mL, 82 mmol). With stirring, the solution was refluxed at 90 °C for 3 h and was cooled to attain an ambient temperature. After the addition of powdered selenium (12.95 g, 164 mmol), the mixture was refluxed and stirred for 6 h, which gave a deep-orange solution, and it was cooled overnight. An off-white crude product was obtained after filtration, which was dissolved in hot dichloromethane. Excess selenium was removed through celite filtration, followed by solvent removal on the rotary evaporator. A white crystalline powder was obtained as the product. Yield: 8.62 g (26%). Elemental analysis: calculated for $C_{12}H_{29}NP_2Se_2$: C, 35.37; H, 7.18; N, 3.44%. Found: C, 35.46; H, 7.18; N, 3.59%. ^{1}H NMR, (δ, $CDCl_3$, 400 MHz): δ = 1.30 (m, 24H, 8 × CH($C\underline{H}_3$)$_2$); 2.73 (m, 4H, 4 × C$\underline{H}$(CH$_3$)$_2$); 3.08 (s, 1H, −NH). ^{13}C NMR: δ = 17.54, 32.19 ppm; ^{31}P {^{1}H} NMR: 90.31 ppm; ^{77}Se NMR: δ = −367.08, −356.26 ppm. $^1J_{P-Se}$ = 751 Hz. MS (ESI) + ve: m/z 408 $[M + H]^+$.

Synthesis of [^{i}Pr$_2$P(S)NHP(Se)^{i}Pr$_2$]. The synthesis of the ligand was performed according to the previous report.[45] Briefly, chlorodiisopropylphosphine (25 g, 26 mL, 164 mmol) in toluene (30 mL) was added slowly into a solution of hot toluene (50 mL) containing 1,1,1,3,3,3-hexamethyldisilazane (13.2 g, 17 mL, 82 mmol). The reaction mixture was stirred and refluxed at 90 °C for 3 h and cooled to room temperature afterward. Powdered selenium (6.48 g, 82 mmol) was added, and stirring continued overnight, after which powdered sulfur (2.63 g, 82 mmol) was added. The mixture was stirred for 6 h, which gave a white solution. This was filtered and dissolved in hot dichlormethane (DCM) to remove excess reactants. From the filtrate, the solvent was removed on the rotavap, and a white crystalline powder was obtained as the product. Yield: 9.71 g (33%). Elemental analysis: calculated for $C_{12}H_{29}NP_2SSe$: C, 40.00; H, 8.11; N, 3.89; S, 8.90%. Found: C, 39.90; H, 8.14; N, 3.88; S, 9.19%. ^{1}H NMR, (δ, $CDCl_3$, 400 MHz): δ = 1.31 (m, 24H, 8 × CH($C\underline{H}_3$)$_2$); 2.48 (m, 2H, Se═P−C$\underline{H}$(CH$_3$)$_2$); 2.73 (m, 2H, S═P−C$\underline{H}$(CH$_3$)$_2$);

https://doi.org/10.1021/acs.inorgchem.2c00460
Inorg. Chem. 2022, 61, 6612−6623

3.20 (s, 1H, −NH). ^{13}C NMR: δ = 17.57, 31.12 ppm; ^{31}P {^{1}H} NMR: 92.56, 89.28 ppm. MS (EI): m/z 361 $[M]^+$.

Synthesis of [^{i}Pr$_2$P(S)NHP(S)^{i}Pr$_2$]. The synthesis of the ligand was performed according to the previous report.[45] Briefly, chlorodiisopropylphosphine (25 g, 26 mL, 164 mmol) in toluene (30 mL) was added slowly into a solution of hot toluene (50 mL) containing 1,1,1,3,3,3-hexamethyldisilazane (13.2 g, 17 mL, 82 mmol). Stirring and refluxing continued for 3 h at 90 °C, and subsequently cooled to room temperature. Powdered sulfur powder (5.26 g, 164 mmol) was added, and the mixture was refluxed with stirring for 6 h. Overnight cooling of the mixture produced a white solution, which was filtered. The residue of white precipitate was purified with CS_2 (2 × 15 mL) and *n*-hexane (15 mL). A white crystalline powder was obtained as the product. Yield: 10.35 g (40%). Elemental analysis: calculated for $C_{12}H_{29}NP_2S_2$: C, 45.99; H, 9.33; N, 4.47; S, 20.42%. Found: C, 46.15; H, 9.42; N, 4.64; S, 20.19%. ^{1}H NMR, (δ, $CDCl_3$, 400 MHz): δ = 1.21 (m, 24H, 8 × CH(C$\underline{H}_3$)$_2$); 2.52 (m, 4H, 4 × C$\underline{H}$(CH$_3$)$_2$); 2.88 (s, 1H, −NH). ^{13}C NMR: δ = 17.28, 31.92 ppm; ^{31}P {^{1}H} NMR: 90.88 ppm. MS (ESI) −ve: m/z 312 $[M - H]^+$.

Synthesis of Complexes. *Synthesis of Mn[(SeP^{i}Pr$_2$)$_2$N]$_2$* ***1***. In redistilled MeOH (35 mL), diselenoimidodiphosphinate ligand (3.00 g, 7.37 mmol) was dissolved and stirred for half an hour, followed by the addition of NaOMe (0.40 g, 7.37 mmol) for in situ deprotonation of the ligand. A yellow solution was observed. Methanolic solution of $MnCl_2$ (0.46 g, 3.68 mmol) was added dropwise, and the solution turned light brown. After stirring for 4 h, a dark-brown solution was obtained, the precipitate was filtered, and dissolved in hot DCM. The hot filtration produced a yellow filtrate, from which the solvent was removed on the rotavap. The product obtained was a crystalline orange powder. Yield: 1.44 g (45%). Elemental analysis calculated for $C_{24}H_{56}MnN_2P_4Se_4$: C, 33.21; H, 6.51; N, 3.23%. Found: C, 33.18; H, 6.49; N, 3.21%. M.Pt: 149 °C. ^{1}H NMR, (δ, $CDCl_3$, 400 MHz): δ = 1.35 (m, 24H, 8 × CH(C$\underline{H}_3$)$_2$); 2.46 (m, 24H, 8 × C$\underline{H}$(CH$_3$)$_2$); ^{13}C NMR: δ = 17.29, 17.96, 32.21 ppm; ^{31}P {^{1}H} NMR: 70.26, 73.31 ppm. MS (EI): m/z 408 $[(SeP^iPr_2)_2N]^+$, m/z 463 $[(SeP^iPr_2)_2N + C_4H_7]^+$, m/z 866 $[Mn\{(SeP^iPr_2)_2N\}_2]^+$.

Synthesis of Mn[(SP^{i}Pr$_2$)(SeP^{i}Pr$_2$)N]$_2$ ***2***. The thioselenoimidodiphosphinate ligand (3.00 g, 8.33 mmol) was added to dry MeOH (30 mL) and stirred for 30 min. Following the addition of NaOMe (0.45 g, 8.33 mmol) and stirring for half an hour to remove the acidic proton, a yellow solution was obtained. Dropwise addition of the methanolic solution of $MnCl_2$ (0.53 g, 4.16 mmol) in 20 mL of MeOH produced a pink solution, which was stirred for 4 h. This was filtered and dissolved in hot DCM, followed by solvent removal under pressure. A crystalline orange powder was obtained as the product. Yield: 1.26 g (39%). Elemental analysis calculated for $C_{24}H_{56}MnN_2P_4S_2Se_2$: C, 37.25; H, 7.30; N, 3.62; S, 8.27%. Found: C, 37.95; H, 7.41; N, 3.71; S, 9.07%. M.Pt: 141 °C. ^{1}H NMR, (δ, $CDCl_3$, 400 MHz): δ = 1.33 (m, 24H, 8 × CH(C$\underline{H}_3$)$_2$); 1.61 (m, 24H, 8 × C$\underline{H}$(CH$_3$)$_2$); ^{13}C NMR: δ = 17.27, 31.11 ppm; ^{31}P {^{1}H} NMR: 89.30, 92.56 ppm. MS (EI): m/z 361 $[\{(SP^iPr_2)(SeP^iPr_2)N\}_2]^+$, m/z 415 $[\{(SP^iPr_2)(SeP^iPr_2)N\}_2 + C_4H_7]^+$, m/z 773 $[Mn\{(SP^iPr_2)(SeP^iPr_2)N\}_2]^+$.

Synthesis of Mn[(SP^{i}Pr$_2$)$_2$N]$_2$ ***3***. In dry MeOH (35 mL), the dithioimidodiphosphinate ligand (3.00 g, 9.57 mmol) was added and stirred for 30 min. NaOMe (0.52 g, 9.57 mmol) was introduced, and the mixture was stirred for half an hour. Methanolic solution of $MnCl_2$ (0.60 g, 4.79 mmol) in 20 mL of MeOH was added dropwise. After 4 h, a whitish-pink solution was obtained. This was filtered and dissolved in hot DCM for the removal of excess reactants. The solvent was removed from the filtrate on the rotary evaporator to obtain a light pink powder. Yield: 1.09 g (34%). Elemental analysis calculated for $C_{24}H_{56}MnN_2P_4S_4$: C, 42.40; H, 8.30; N, 4.12; S, 18.86%. Found: C, 42.36; H, 8.27; N, 4.09; S, 18.21%. M.Pt: 139 °C. ^{1}H NMR, (δ, $CDCl_3$, 400 MHz): δ = 1.34 (m, 24H, 8 × CH(C$\underline{H}_3$)$_2$); 1.59 (m, 24H, 8 × C$\underline{H}$(CH$_3$)$_2$); ^{31}P {^{1}H} NMR: 94.40 ppm. MS (EI): m/z 312 $[(SP^iPr_2)_2N]^+$, m/z 367 $[(SP^iPr_2)_2N + C_4H_7]^+$, m/z 679 $[Mn\{(SP^iPr_2)_2N\}_2]^+$.

Synthesis of Cu[(SeP^{i}Pr$_2$)$_2$N]$_2$ ***4***. While stirring, the imidodiselenodiphosphinate ligand (3.00 g, 7.37 mmol) was dissolved in dry MeOH (30 mL), and subsequently, NaOMe (0.40 g, 7.37 mmol) was added with further stirring for half an hour. Dropwise addition of $CuCl_2$ (0.50 g, 3.68 mmol) solution in MeOH (20 mL) resulted in a brown coloration of solution. An ox-blood solution was obtained after 4 h, which was filtered, and the residue was dissolved in hot DCM. The solution was filtered, which gave an off-green filtrate, followed by solvent removal on the rotary evaporator. A crystalline greenish product was obtained. Yield: 1.26 g (39%). Elemental analysis calculated for $C_{24}H_{56}CuN_2P_4Se_4$: C, 32.89; H, 6.44; N, 3.20%. Found: C, 31.22; H, 6.04; N, 2.98%. M.Pt: 147 °C. ^{1}H NMR, (δ, $CDCl_3$, 400 MHz): δ = 1.24, 2.18, 5.31 ppm; ^{13}C NMR: δ = 17.53, 31.13, 32.63 ppm; ^{31}P {^{1}H} NMR: 52.12 ppm. MS (EI): m/z 409 $[(SeP^iPr_2)_2N]^+$, m/z 808 $[Cu\{(SeP^iPr_2)_2N\}_2 - 2PH_3]^+$, m/z 873 $[Cu\{(SeP^iPr_2)_2N\}_2 - 3]^+$.

Synthesis of Cu[(SP^{i}Pr$_2$)(SeP^{i}Pr$_2$)N]$_2$ ***5***. While stirring for 30 min, the thioselenoimidodiphosphinate ligand (3.50 g, 9.71 mmol) was dissolved and stirred in dry MeOH (30 mL), followed by the addition of NaOMe (0.52 g, 9.71 mmol) to deprotonate the ligand. Through dropwise addition, $CuCl_2$ (0.65 g, 4.86 mmol) in 20 mL of MeOH was added to the solution, which turned brown. This was stirred for 4 h and filtered. Dissolution in hot DCM and subsequent filtration produced a dark-green filtrate, from which the solvent was removed under vacuum. A crystalline yellowish-green product was obtained. Yield: 0.82 g (22%). Elemental analysis calculated for $C_{24}H_{56}CuN_2P_4S_2Se_2$: C, 36.84; H, 7.22; N, 3.58; S, 8.18%. Found: C, 35.47; H, 7.02; N, 3.54; S, 8.36%. M.Pt: 136 °C. ^{1}H NMR, (δ, $CDCl_3$, 400 MHz): δ = 1.24, 2.16, 2.97 ppm; ^{13}C NMR: δ = 17.28, 31.83 ppm; ^{31}P {^{1}H} NMR: 54.38, 63.03 ppm. MS (EI): m/z 361 $[\{(SP^iPr_2)(SeP^iPr_2)N\}_2]^+$, m/z 784 $[Cu\{(SP^iPr_2)(SeP^iPr_2)N\}_2 + 2]^+$.

Synthesis of Cu[(SP^{i}Pr$_2$)$_2$N]$_2$ ***6***. In dry MeOH (30 mL), the dithioimidodiphosphinate ligand (2.50 g, 7.98 mmol) was dissolved and stirred for half an hour, after which NaOMe (0.43 g, 7.98 mmol) was added for in situ deprotonation. A solution of $CuCl_2$ (0.54 g, 3.99 mmol) in MeOH (20 mL) was added in drops, and violet coloration was observed. The solution was stirred for 4 h, which turned off-white in color. After filtration, excess reactants were removed through dissolution in hot DCM. From the filtrate, the solvent was removed under vacuum, and a crystalline creamy product was obtained. Yield: 0.82 g (30%). Elemental analysis calculated for $C_{24}H_{56}CuN_2P_4S_2Se_2$: C, 41.87; H, 8.21; N, 4.07; S, 18.59%. Found: C, 37.33; H, 7.32; N, 3.65; S, 20.73%. M.Pt: 139 °C. ^{1}H NMR, (δ, $CDCl_3$, 400 MHz): δ = 1.26, 1.60, 2.16 ppm; ^{13}C NMR: δ = 16.82, 31.47; ^{31}P {^{1}H} NMR: 58.35 ppm. MS (EI): m/z 313 $[(SP^iPr_2)_2N]^+$, m/z 375 $[Cu(SP^iPr_2)_2N]^+$, m/z 681 $[Cu\{(SP^iPr_2)_2N\}_2 - H]^+$.

Melt Reactions. Under inert conditions, 0.6 mmol of the precursor was placed in a ceramic boat in a glass tube. The tube was inserted inside the tube furnace. One end of the tube was sealed using a rubber septum, and the other end of the tube was connected to Schlenk-line. The tube was evacuated three times and filled each time with an inert atmosphere of nitrogen. The furnace was heated at 10 °C min^{-1} to 500 °C (and 550 °C) for 1 h. After cooling to room temperature, the deposited sample was removed and ground prior to characterization. As the complexes were sublimating in nature, some deposition was also observed on the wall of the reactor tube.

Characterization of the Complexes. Using Leco CHNS-932 or El Vario III elemental analyzers, CHN analyses were done at the Microanalytical section of the Institute of Organic Chemistry and Macromolecular Chemistry (IOMC), Friedrich-Schiller-Universität, Jena, Germany. Thermogravimetric analysis (TGA) measurements were performed using the NETZSCH STA 409F PC/PG DTA/TG model with a heating rate of 5 K min^{-1}. A Bruker Avance (III) 400 MHz FT-NMR spectrometer was used for nuclear magnetic resonance (NMR) spectra analyses, with either deuterated chloroform or toluene as the solvent. ^{1}H NMR spectra analyses were reported in reference to tetramethylsilane Me_4Si, while ^{31}P NMR spectra analyses were referenced to H_3PO_4. The melting point was recorded on a Gallenkamp melting point apparatus. Mass spectrometry (MS) spectra were recorded on a Bruker MAT SSQ 710 spectrometer by using electron ionization or electron spray ionization. The intensity data for the compounds **1**, **2**, and **HL3** were collected on a Nonius

https://doi.org/10.1021/acs.inorgchem.2c00460
Inorg. Chem. 2022, 61, 6612−6623

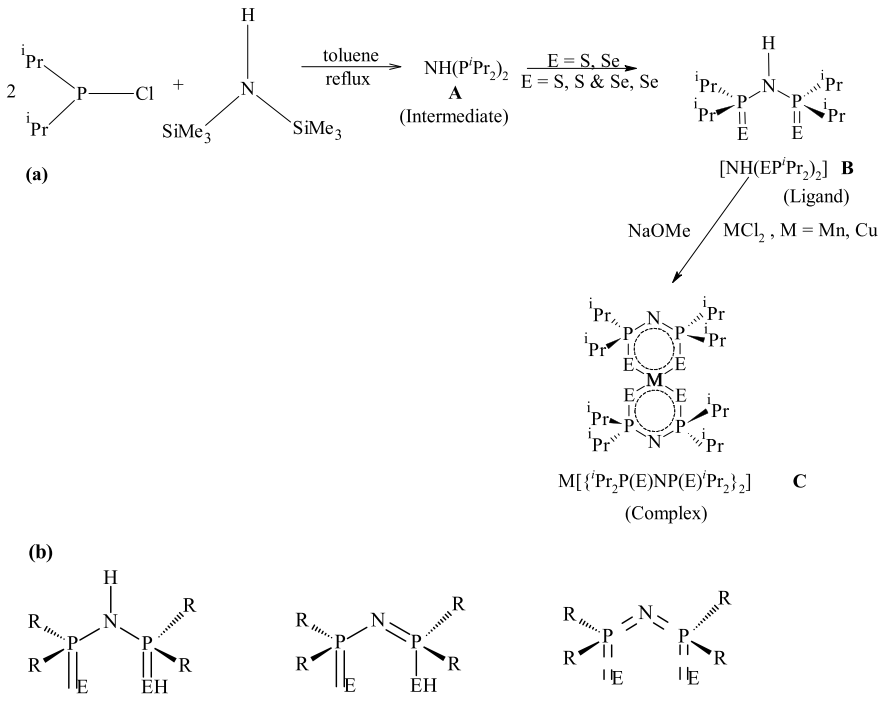

Figure 1. (a) Schematic diagram for the synthesis of ligands and complexes of manganese and copper. (b) Anionic chelate forms of the dichalcogenoimidodiphosphinate ligand. (**A** = intermediate; **B** = ligand; and **C** = complex).

Table 1. Crystal Data and Refinement Details for Compounds 1, 2, and HL3

compound	1	2	HL3
formula	$C_{24}H_{56}MnN_2P_4Se_4$	$C_{24}H_{56}MnN_2P_4S_2Se_2$	$C_{12}H_{29}NP_2S_2$
fw (g·mol^{-1})	867.36	773.56	313.42
T/°C	−140(2)	−140(2)	−140(2)
crystal system	triclinic	triclinic	monoclinic
space group	$P\bar{1}$	$P\bar{1}$	$P2_{1/c}$
a/Å	9.3488(2)	9.2937(2)	14.1645(3)
b/Å	12.9203(3)	12.8637(2)	10.4773(2)
c/Å	16.3217(4)	16.3148(3)	11.8740(3)
α/°	79.041(1)	79.075(1)	90
β/°	77.937(1)	78.012(1)	105.394(1)
γ/°	70.258(1)	69.588(1)	90
V/Å^3	1799.27(7)	1773.48(6)	1698.95(7)
Z	2	2	4
ρ (g·cm^{-3})	1.601	1.449	1.225
μ (cm^{-1})	46.07	27.4	4.85
measured data	20,400	17,723	12,031
data with $I > 2\sigma(I)$	6364	7045	3503
unique data (R_{int})	8155(0.0736)	8051(0.0222)	3896(0.0353)
wR_2 (all data, on F^2)[a]	0.1327	0.0654	0.0868
R_1 ($I > 2\sigma(I)$)[a]	0.0659	0.0305	0.0385
S[b]	1.071	1.054	1.058
res. dens./e·Å^{-3}	1.213/−0.849	0.399/−0.319	1.156/−0.456
absorpt. method	multi-scan	multiscan	multiscan
absorpt. corr. $T_{min/max}$	0.6034/0.7456	0.6263/0.7456	0.7128/0.7456
CCDC No.	2069431	2069432	2069433

[a]Definition of the *R* indices: $R_1 = (\Sigma||F_o| - |F_c||)/\Sigma|F_o|$; $wR_2 = \{\Sigma[w(F_o^2 - F_c^2)^2]/\Sigma[w(F_o^2)^2]\}^{1/2}$ with $w^{-1} = \sigma^2(F_o^2) + (aP)^2 + bP$; $P = [2F_c^2 + \mathrm{Max}(F_O^2]/3$. [b]$s = \{\Sigma[w(F_o^2 - F_c^2)^2]/(N_o - N_p)\}^{1/2}$.

KappaCCD diffractometer using graphite-monochromated Mo-K$_\alpha$ (λ = 0.71073 Å) radiation. Data were corrected for Lorentz and polarization effects; absorption was taken into account on a semiempirical basis using multiple scans.[46−48] The structures were solved using direct methods (SHELX-2014[49]) and refined by full-matrix least-squares techniques against Fo.[2] All nonhydrogen atoms were located in the difference density map and refined anisotropically with SHELX-2014.[49] All hydrogen atoms were included as idealized contributors in the least-squares process. Their positions were calculated using a standard riding model with SHELX-2014. The amine N−H was located in the difference density map and refined isotropically. Compound **2** was refined to account for the site disorder

https://doi.org/10.1021/acs.inorgchem.2c00460
Inorg. Chem. 2022, 61, 6612−6623

of the Se/S ligand donor atoms with a final site occupancy factor of 17:83. Mercury[50] was used for visualizing and analyzing structures.

Characterization of Deposited Metal Chalcogenides. *p*-XRD patterns were measured at room temperature using a Bruker AXS D8 Advance diffractometer supplied with nickel-filtered Cu-Kα radiation, at 40 kV and 40 mA (λ = 1.5418 Å). Images for TEM and SAED were measured on a JEOL 1400 TEM equipment fitted with a Gatan camera at an accelerating voltage of 120 kV. Ethanol suspensions of melt products were diluted and sonicated, followed by evaporation on Formvar-coated copper grids (150 mesh) before analyses. The soft Imaging Systems program was used to process the resultant images. SEM, EDX, and elemental mapping were performed on a ZEISS EVO LS 15 equipment connected to an Oxford detector at 20 kV. The deposited powders were added in small pieces onto a carbon tape connected to an SEM stub. Before analyses were performed, samples were carbon-coated using a Quorum coater (Q150TE).

RESULTS AND DISCUSSION

The ligands and the complexes were synthesized in a one-pot route according to the synthetic route depicted in Figure 1a. The dichalcogenoimidodiphosphinate ligands were synthesized by refluxing chlorodiisopropylphosphine and hexamethyldisilazane to produce $[NH(P^iPr_2)_2]$ (**A**), after which the addition of stoichiometric amounts of sulfur, selenium or equimolar sulfur, and selenium produced the ligand $[NH(EP^iPr_2)_2]$ (**B**). This ligand contains an acidic N−H proton, which can be easily deprotonated to form anionic chelate complexes, as shown in Figure 1b. The reaction of the ligand $[NH(EPR_2)_2]$ with appropriate metal (Cu, Mn) salts formed the neutral complexes (**C**) with the general formula ML_2.

X-Ray Crystal Structure and Density Functional Theory. The dithioimidodiphosphinate ligand had been studied by Cupertino *et al.*, with the previous report showing the ligand in the $P2_1/a$ space group.[45b] The present structure is in the $P2_1/c$ space group, that is, a new polymorph, is free from the positional disorder in the terminal methyl groups associated with the previously reported structure. In addition to being a new polymorph free of disorders, the structure presented herein was determined at cryogenic temperature, resulting in an improved C−C bond accuracy and an improved R-factor. Crystallographic data as well as structure solution and refinement details are summarized in Table 1.

The ligand molecule in the asymmetric unit (Figure 2) shows that it has adopted a somewhat unusual gauche-configuration as represented by the S1−P1···P2−S2 "torsion" angle, which measures 83.26(3)°. This is in contrast to other derivatives of the ligand such as the isobutyl analogue, *P*,*P*-diisobutyl-*P*′,*P*′-disecbutyldithioimidodiphosphinate,[51] which shows the expected anticonfiguration rotamer. The antirotamer is typically lower in energy in most chemical systems.[52]

The ligand forms one-dimensional hydrogen-bonded chains in the solid-state, which are colinear with the crystallographic *c*-axis. This hydrogen-bonded chain (Figure 2) is supported by hydrogen bonds between the amine NH and the sulfur atom of an adjacent molecule, N1···S1 (3.543(2) Å), H1N···S1 (2.74(2) Å), and N1−H1N (0.80(2) Å). The length of this interaction is significantly shorter (by 0.256 Å) than the sum of the van der Waals radii of the interacting non-H atoms. Although the interaction length does not necessarily correlate linearly with interaction strength because of packing constraints in the lattice, the short distance coupled with a near-optimum hydrogen bond angle of 173(3)° suggests that the bond is likely to be moderately strong. The structure also shows two intramolecular C−H···S interactions between the

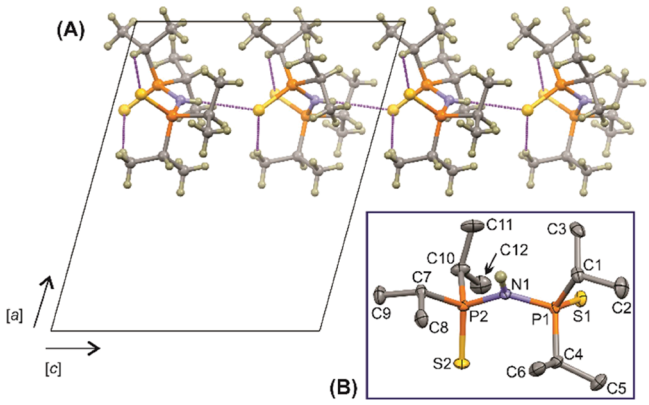

Figure 2. (A) One-dimensional hydrogen-bonded chain formed by the ligand **HL3** in the solid state viewed down the *b*-axis. The chain is colinear with the *c*-axis and is supported by hydrogen bonds between the amine NH (H-bond donor) and the sulfur atom of an adjacent molecule (H-bond acceptor). Symmetry code: x, $1/2 - y$, $-1/2 + z$. [B] Labeled asymmetric unit of **HL3** showing displacement ellipsoids at the 50% probability level; alkyl hydrogen atoms have been excluded.

isopropyl groups and the sulfur atoms. These C−H···S interactions (2.786 and 2.793 Å) are again significantly shorter than the sum of the van der Waals radii (>0.2 Å shorter) in this instance; this interaction distance is directly limited by the geometry of the ligand, and no inference of interaction strength would be valid. The P1−S1 bond length, 1.9591(8) Å, is shorter than the P2−S2 bond length, 1.9494(6) Å. This is likely a consequence of the electronic influence of hydrogen bonding. The selenium analogue of the free ligand shows a similar elongation of the P−Se bond when the selenium atom is involved in hydrogen bonding.[44] The mean P−N bond length of the ligand measures 1.692(3) Å. This is relatively short but falls within the range for a P−N single bond. The mean P═S bond length, 1.954(1) Å, is short and is indicative of double-bond character. The N−P−S bond angles are slightly more obtuse than the ideal angle for an sp^3-hybridized atom with a mean bond angle of 114.8(8)°.

A search of the Cambridge Structural Database (CSD) showed that although imidodiphosphinate ligands with S_2- and Se_2-donor atom sets are well studied, there are comparatively a few reported structures of mixed Se/S donor imidodiphosphinate ligands. The bis((diisopropylthiophosphoryl)-(diisopropylselenophosphoryl)amido-S,Se) metal chelates are limited to Pb^{2+}, Zn^{2+}, Ni^{2+}, Pt^{2+}, Ga^{3+}, and In^{3+}.[45a,53−55] The manganese(II)-coordinated compound **2** is thus unique. Bis(P,P,P′,P′-tetraisopropyldiselenoimidodiphosphinato) metal chelates with various divalent metal ions including, but not limited to, Ni^{2+}, Hg^{2+}, Pt^{2+}, Cd^{2+}, Sn^{2+}, Pb^{2+}, and Co^{2+} have been reported;[31,56−59] the Mn^{2+} chelate is, however, previously unknown.

The bidentate ligands HL1 and HL2 both readily coordinate Mn^{2+} with concomitant deprotonation of the acidic amine groups. The bis(imidodiphosphinato) chelates are thus neutral with the Mn^{2+} ion adopting a distorted tetrahedral geometry, as shown in Figure 3. Chelation of the bidentate ligands leads to a six-membered chelate ring, which has adopted a half-chair conformation; this is consistent with related sulfur and selenium analogues.[45,51] The ligand has a large bite, which gives a mean intraligand Se−Mn−Se bond angle of 112.1(6)°. The interligand Se−Mn−Se bond angle of **1** is more acute

https://doi.org/10.1021/acs.inorgchem.2c00460
Inorg. Chem. 2022, 61, 6612−6623

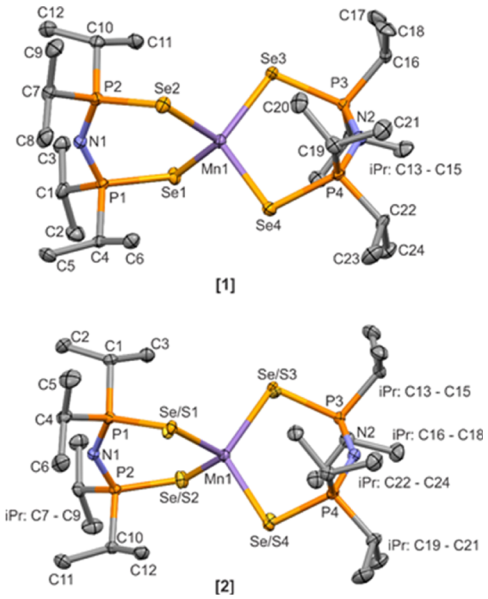

Figure 3. Labeled displacement ellipsoid plots rendered at the 50% probability level for the manganese(II) chelates of (top) compound **1** and (bottom) compound **2**. Both chelates show a distorted tetrahedral coordination geometry at the metal center. Compound **2** shows the site disorder of the Se and S donor atoms with a site occupancy ratio of 17:83. H-atoms are omitted for clarity.

than the optimum angle for a tetrahedral metal ion, with a mean of 109.0(6)°. The Mn−Se bond lengths show one shorter and one longer bond between the metal and the selenium atoms of each ligand. This may suggest that one of the coordinating atoms carries a partial negative charge, although the P═Se bond lengths show no statistical difference in length to support this argument. The bond lengths and bond angles describing the coordination sphere are summarized in Table 2. The P−N bond lengths are shorter in the metal

Table 2. Selected Geometric Parameters Describing the Coordination Sphere of the Manganese(II) Chelates 1 and 2

1		2	
bond	geometry (Å or °)	bond	geometry (Å or °)
Mn1−Se1	2.559(1)	Mn1−Se1[a]	2.54(1)
Mn1−Se2	2.545(1)	Mn1−S1[a]	2.45(2)
Mn1−Se3	2.556(1)	Mn1−Se2[a]	2.55(1)
Mn1−Se4	2.545(1)	Mn1−S2[a]	2.47(2)
Se1−Mn1−Se2[b]	111.68(4)	Se1−Mn1−S2[a,b]	110.1(4)
Se3−Mn1−Se4[b]	112.47(4)	Se3−Mn1−S4[a,b]	111.2(5)
Se1−Mn1−Se3[c]	110.70(4)	Se1−Mn1−S3[a,c]	107.9(4)
Se1−Mn1−Se2[c]	111.68(4)	Se1−Mn1−S2[a,c]	107.9(5)

[a]These are the mean Mn−S/Se bond lengths and bond angles, accounting for the site disorder. [b]These are intraligand bond angles. [c]These are interligand bond angles.

chelate **1** than the equivalent bonds in the free ligand, 1.588(3) versus 1.690(4),[43a] while the P═S bond lengths are significantly longer in the metal chelate (2.178(3)) than in the free ligand (2.100(2)). These changes in the bond length illustrate the effects of electron delocalization as a consequence of ligand deprotonation and the electron-withdrawing effects of the metal ion. The P−N−P bond angle is ca. 10° more obtuse in the metal chelate than the free ligand. The reason for this is not immediately apparent, but it has been reported in some instances with related metal chelates.[45b]

The mixed Se/S donor ligand in compound **2** shows the site disorder of the coordinating Se/S atoms, and a similar site disorder has been previously reported for this class of ligands.[45a] As is the case with the selenium donor chelate of Mn^{2+}, the ligands have adopted a half-chair configuration, and the metal ion has maintained the expected tetrahedral geometry. The similar ligand architecture again leads to a large ligand bite, and the intraligand Se−Mn−S bond angle is more obtuse than the interligand Se−Mn−S bond angle; the same was noted in the Se_2-donor ligand. The P−N−P bond angle in the mixed donor ligand measures 140.1(2)°, this again highlights the similarity of the ligand structures with the equivalent parameter in the Se_2-donor ligand measuring 141.2(5)°. The geometric parameters describing the coordination spheres of both compounds **1** and **2** are summarized in Table 2.

The gauche configuration of the ligand in the solid state prompted a study of the energies of the various rotamers of **HL3** with molecular simulations using DFT methods. These simulations were performed using Gaussian 09 W.[60] The X-ray coordinates were used for the initial input structure. The lowest energy conformations were determined through geometry optimization. Frequency simulations were completed for all optimized structures. All simulations were run at the CAM-B3LYP/6-311G level of theory, and single first polarization and diffuse functions (d, p) were also added to the basis set to improve accuracy. Input files were prepared, and output files were analyzed using GaussView 5.0.[61] The frequency simulations suggested that the geometry optimizations were true minima on the global potential energy surface based on a lack of negative frequency eigenvalues. The solid-state structure of **HL3** showed it to be in the gauche configuration with a S1−P1···P2−S2 torsion angle measuring 83.26(3)°. The total energy of various molecular configurations as a function of the S1−P1···P2−S2 torsion angles were calculated using a scan simulation (rotations were effected in 15° increments for a total of 24 steps).

The molecular simulations showed that a configuration with an approximate anticonfiguration, as represented by a S1−P1···P2−S2 "torsion" angle of −145.059°, is only marginally higher in energy, by 0.59 kJ mol^{-1}, when compared to the optimized gauche configuration with the equivalent torsion measuring −235.059°; these two low energy configurations are illustrated in Figure 4. Analysis of the frequency eigenvalues showed that the gauche configuration had no negative frequencies, while the "anti" configuration had a single negative frequency. This single negative frequency indicates that the structure is a saddle point on the potential energy surface. The very low energy barrier between these two rotamers suggests that the slight energy penalty associated with the approximate anticonfiguration in the solid-state could be offset by energy gains through more favorable packing in the crystal lattice in some cases. These data illustrate why both configurations are noted in the CSD. The influence of the S1−P1···P2−S2 torsion angle on the free energy of the molecule in vacuo is presented in Figure 4.

The scan simulations show that both gauche and anticonfigurations are low-energy rotamers. The eclipsed configuration is significantly higher in energy. Analysis of the space-filling model rendered using the van der Waals radii of the atoms (Figure S1, ESI) shows that this is likely the result of

https://doi.org/10.1021/acs.inorgchem.2c00460
Inorg. Chem. 2022, 61, 6612−6623

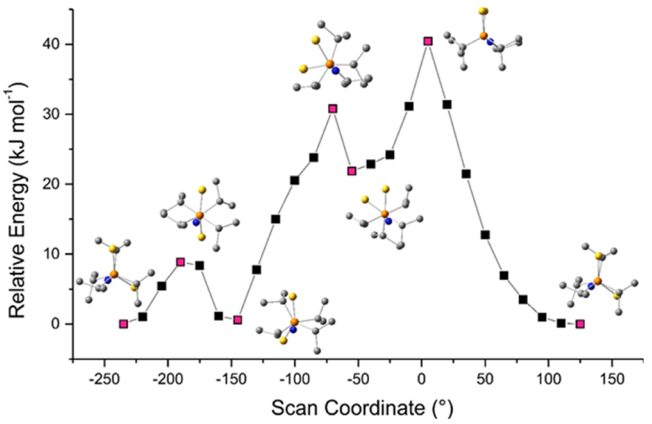

Figure 4. Relative energies of compound **HL3** as a function of the S1−P1···P2−S2 torsion angle. Energy maxima and minima are highlighted in magenta with their corresponding structures. The simulations were run using a scan operation with 24 steps at 15° intervals. The lowest energy conformation with a torsion angle of −235° is used as the energy reference point. Hydrogen atoms are omitted for clarity.

both nonbonded repulsion between the lone electron pairs on the sulfur atoms as well as steric effects of the interacting isopropyl substituents.

Thermogravimetric Analysis. The solid-state stability of the complexes was investigated by thermogravimetric analysis (TGA). All the complexes **1**−**6** exhibited clean decomposition, as revealed by their rapid weight loss and a single-step decomposition pattern (Figure S2 and S3, ESI). [Mn{$(SeP^iPr_2)_2N$}$_2$] **1** showed a clean sublimation between 285 and 410 °C, with 7% residual mass. [Mn{$(SP^iPr_2)(SeP^iPr_2)$N}$_2$] **2** decomposed between 275 and 408 °C with a final residue of 9%. Between 300 and 405 °C, a rapid weight loss occurred in [Mn{$(SP^iPr_2)_2N$}$_2$] **3**, having a final residue of 0%. With a residual mass of 20%, single-step decomposition occurred in [Cu{$(SeP^iPr_2)_2N$}$_2$] **4** between 300 and 375 °C. A similar single-step decomposition pattern was observed in [Cu{$(SP^iPr_2)(SeP^iPr_2)N$}$_2$] **5** with a rapid weight loss between 300 and 375 °C, and a final residue of 22%. Likewise, similar to [Mn{$(SP^iPr_2)_2N$}$_2$], the dithio-analogue of copper [Cu{$(SP^iPr_2)_2N$}$_2$] **6** also sublimed completely in a single-step between 325 and 380 °C, and continues to sublime with a further increase in temperature. It can be seen that the thio analogues of both complexes are more easily sublimed when compared to selenium or mixed thio-/seleno-complexes. The alkyl derivatives of dichalcogenoimidodiphosphinate complexes are well known for their sublimating nature, and for the same reason, they have been precursors of choice for the deposition of different metal chalcogenide thin films by low-pressure chemical vapor deposition (LP-CVD).[54,62,63] Generally, for metal−organic precursors, the percentage of the residual mass can indicate the nature of the metal chalcogenide phase formed. However, because of sublimation, the determination of the nature of the metal chalcogenide formed on the decomposition of the precursor is impossible to determine via the percentage of the residual material.

Structural Analysis of the Metal Chalcogenides. As the TGA indicated that all the complexes decomposed around 400 °C, therefore, for better crystallinity, the pyrolysis experiments were carried out at 500 and 550 °C. The solvent-less thermolysis of all complexes **1**−**6** at 500 and 550 °C produced black powders, which were pulverized and characterized by *p*-XRD. The black powder obtained from the diseleno-analogue **1**, at 500 °C, produced no diffraction pattern, whereas decomposition at a higher temperature of 550 °C with *p*-XRD analysis confirmed the deposition of cubic manganese selenide, $MnSe_2$ (ICDD 03-065-3336, $a = b = c =$ 6.4300 Å, space group number *Pa*-3(205)) (Figure 5a). The

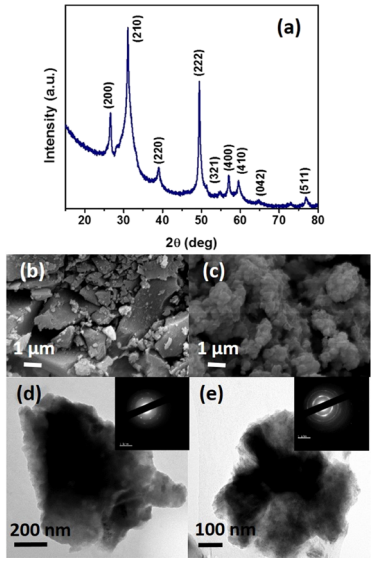

Figure 5. (a) X-ray diffractogram of cubic $MnSe_2$ obtained from the pyrolysis of complex (**1**) at 550 °C. (b,c) SEM images of manganese selenide prepared at 500 and 550 °C, respectively. TEM images of manganese selenide prepared at (d) 500 °C and (e) 550 °C, respectively (inset shows the SAED pattern).

obtained lattice parameter of a = 6.4287 Å matches the literature-reported value (Table S1, ESI). The observed reflections occurred at 2θ values of 27.37°, 31.22°, and 49.89°, which corresponded to (200), (210), and (222) planes. The morphologies of the deposited materials and composition were investigated by SEM and EDAX. Manganese selenide obtained from complex **1** showed sheet-like structures arranged in a random orientation, both at 500 and 550 °C (Figure 5b,c). However, the particles were more agglomerated at a higher temperature. The composition determination by EDX analysis at 500 °C indicated selenium-deficient compound with the Mn:Se ratio as 57.9%:42.1%. As the p-XRD of this sample showed amorphous nature, it was difficult to determine the exact phase; however, EDX analysis indicated that Mn and Se are present closer to 1:1 ratio, which suggests the formation of the MnSe phase. In addition, the elemental mapping shows the presence of both manganese and selenium uniformly distributed in the sample (Figure S4). Meanwhile, the composition of manganese selenide obtained from same complex **1**, at 550 °C, indicated the presence of Mn and Se in the 37.9%:62.1% ratio, respectively. Phosphorus was also observed as an impurity. Previous reports indicated that the use of these ligands for the deposition of thin films by aerosol-assisted chemical vapor deposition (AACVD) or LPCVD also resulted in phosphorus contamination.[18b,64] In addition, it was observed that the amount of phosphorus as an impurity varied from precursor to precursor, ranging from a trace amount of phosphorus to as high as 10%. Mn and Se are approximately present in 1:2 ratio, which is in accordance with the p-XRD

https://doi.org/10.1021/acs.inorgchem.2c00460
Inorg. Chem. 2022, 61, 6612−6623

analysis that indicated the formation of the $MnSe_2$ phase. $MnSe_2$ is an important two-dimensional layered material, and the morphology was also analyzed via TEM analysis, which showed irregular sheet-like structures aggregated together (Figure 5d,e). The selected area electron diffraction (SAED) pattern showed diffused rings for both samples (inset (Figure 5 d,e)), indicative of their amorphous nature, and is in agreement with the p-XRD data.

For the dithio analogue of Mn **3**, although no diffraction pattern was observed at 500 °C, however, cubic manganese sulfide, MnS (ICDD 03-065-0891, $a = b = c = 5.2190$ Å, space group number $Fm\text{-}3m(225)$) was deposited at 550 °C (Figure S5(a)). Although the intensity of the peaks was very low, the lattice parameter (determined by taking into account the low-intensity peaks) of $a = 5.2185$ Å matches the literature value (Table S1, ESI). The low-intensity diffraction peaks were observed at 34.71° and 49.79°, having (200) and (220) planes, respectively (Figure S5(a)). As the *p*-XRD analysis showed amorphous behavior and inconclusive of the formation of MnS, the formation of MnS was also confirmed by EDX and elemental mapping. The elemental mapping confirmed the presence of uniformly distributed Mn and S (Figure S6), and EDX analysis indicates that the product is sulfur-deficient with a Mn:S ratio of 68%:32%, respectively, at 550 °C. The presence of phosphorus as an impurity was also observed. The morphology of particles showed the formation of irregular sheetlike structures at both temperatures as indicated by SEM and TEM analyses (Figure S5(b–e)). Moreover, lateral growth was observed over the sheets, which makes the sheets thicker. The SAED pattern showed diffused rings, which indicates amorphous behavior and agrees with the p-XRD analysis.

Because complex **2** contains both sulfur and selenium atoms, it was used in anticipation of forming mixed thio-/seleno-alloy. Complex **2** was also decomposed at similar temperatures, that is, 500 and 550 °C. The diffraction peaks were located in between the peaks for MnS and MnSe (Figure 6a). Both binary MnS and MnSe exist in the cubic crystal structure and display similar reflections of planes. A slight displacement of the peaks may indicate the successful formation of MnSSe alloy. The shifting of peaks is observed due to the fact that sulfur is smaller in size than selenium; therefore, when sulfur is incorporated into the crystal lattice of MnSe, it changes the lattice parameters. As the theta value is inversely proportional to d-spacing, a shift toward a higher theta value is expected. The peaks were obtained at 2θ values of 33.17°, 47.59°, and 59.00°, with the preferred orientation along the (200) plane. The diffraction patterns were sharp, intense, and clearly visible at both pyrolytic temperatures.

The presence of all the atoms, that is, Mn, S, and Se, was also confirmed by EDX analysis and elemental mapping (Figure 6d). The analysis confirmed the formation of alloyed MnSSe with a ratio of the elements, that is, Mn:Se:S as 27%:48%:25% at 500 °C. The elemental mapping confirmed the uniform distribution of all the elements. The morphology was not different from manganese sulfide and selenide prepared by complexes **1** and **3**. Both SEM (Figure 6b,c) and TEM (Figure 6e,f) analyses show the formation of irregular sheet-like structures with some stacking and agglomeration. SAED of the samples showed defined spots, which indicates better crystallinity and is also supported by the *p*-XRD data.

Likewise, the solid-state pyrolysis of the copper complexes was also investigated. The decomposition of complex **4** at 500

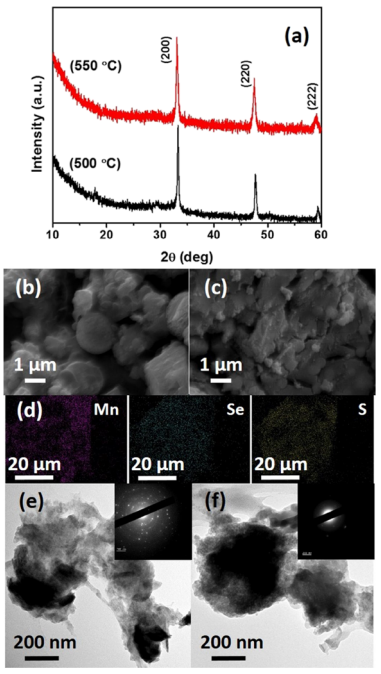

Figure 6. (a) X-ray diffractograms of manganese sulfo-selenide from complex (**2**), at 500 and 550 °C. (b,c) SEM images of manganese sulfo-selenide prepared at 500 and 550 °C, respectively. (d) Elemental mapping and (e,f) TEM images of manganese sulfo-selenide prepared at 500 and 550 °C, respectively (inset shows the SAED pattern).

°C yielded pure phase of cubic copper selenide, $Cu_{2-x}Se$. The intensity profile of the diffraction pattern and the observed lattice parameter matches well with the standard pattern (ICDD 00-006-0680, $a = b = c = 5.7390$ Å, observed lattice parameter of $a = 5.7435$ Å) (Table S1, ESI) (Figure 7a). The peaks were sharp and intense, indicating the crystalline nature of the synthesized material. The formation of the selenium-

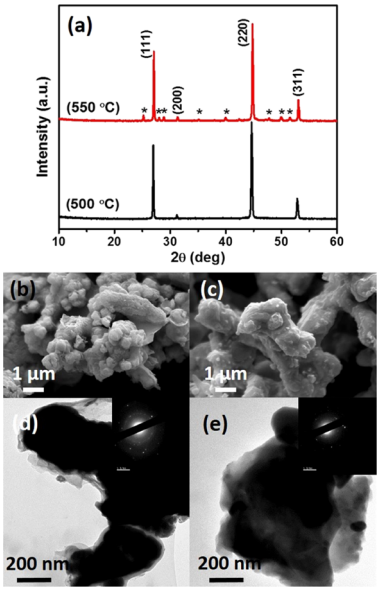

Figure 7. (a) X-ray diffractograms of copper selenide from complex **4**, at 500 and 550 °C (* indicates the presence of Cu_3Se_2 phase). (b, c) SEM images of copper selenide prepared at 500 and 550 °C, respectively. (d,e) TEM images of copper selenide prepared at 500 and 550 °C, respectively (inset shows the SAED pattern).

https://doi.org/10.1021/acs.inorgchem.2c00460
Inorg. Chem. 2022, 61, 6612–6623

deficient phase is facilitated probably due to high partial pressure associated with chalcogenides and also easy reducibility of copper at high temperatures. With an increase in decomposition temperature to 550 °C, low-intensity diffraction peaks of another selenium-deficient phase, that is, Cu_3Se_2 (ICDD 01-071-0045) started to appear as an impurity phase. Copper chalcogenides exist in various compositions/phases, and a slight variation in the reaction conditions can induce the formation of a different phase. For such materials, obtaining a phase-pure product is a challenge, and in this case, a temperature of 500 °C is an optimal temperature for phase-pure $Cu_{2-x}Se$.

Copper chalcogenides show a range of morphologies, such as spherical, sheet-like, discotic, hexagonal, or multifaceted polyhedral nanoparticles. Therefore, the morphology was analyzed by SEM and TEM analyses and similar to manganese chalcogenides, that is, without any defined shape, and no control over shape and size was observed in the absence of surfactants (Figure 7b–e). SEM images showed particles with irregular morphology, while TEM analysis indicated the formation of sheetlike structures with sizes in the micron range. There was no significant effect of temperature on morphology or size, being polydispersed at both temperatures. The composition was further confirmed via EDX analysis, which showed the percentage composition of copper and selenium to be 66.9 and 33.1%, respectively, for pure $Cu_{2-x}Se$ deposited at 500 °C. The ratio confirms the presence of copper and selenium in a desired 2:1 ratio. The elemental mapping also confirmed that both elements were well distributed in the synthesized product (Figure S7).

Similarly, the dithio-analogue of copper complex **6** was thermolyzed under similar conditions to obtain copper sulfide. However, at both temperatures, that is, at 500 and 550 °C, a mixture of hexagonal copper sulfide CuS (ICDD#01-075-2236) and orthorhombic copper sulfide Cu_2S (ICDD#00-012-0227) was observed (Figure S8(a)). As mentioned earlier, copper chalcogenides exist in various phases, and a slight change in the stoichiometry or reaction conditions may favor the formation of a different phase. No defined morphology was observed at both temperatures either by SEM or TEM analysis, and agglomerated platelets like structures were formed (Figure S8(b–e)).

After dithio- and diseleno-analogues, a mixed thio-/seleno-complex of copper **5** was pyrolyzed to observe whether it formed the alloyed copper sulfo-selenide. The diffraction pattern showed that at both decomposition temperatures, that is, 500 and 550 °C, tetragonal copper selenide and Cu_3Se_2 (ICDD#00-019-0402, $a = b = 6.4060$ Å, $c = 4.2820$ Å) were deposited as a parent phase (Figure 8a). The intensity profile slightly changed with the change in temperature, and at higher temperature, maximum diffraction peaks were observed. The peaks were slightly shifted to higher theta values, which may indicate the presence of sulfur in the crystal lattice. However, only *p*-XRD analysis was insufficient to confirm the presence of sulfur. Therefore, EDX analysis and elemental mapping were performed to observe the presence of sulfur. Elemental mapping clearly showed the presence of sulfur, although relatively in a small amount, along with copper and selenium (Figure 8d). EDX analysis showed the elemental composition to be Cu, 65%; Se, 30.5%; S, 4.5% at 500 °C. It is interesting to note that the diseleno-analogue yielded the $Cu_{2-x}Se$ phase at 500 °C and started to transform to the Cu_3Se_2 phase with an increase in temperature, whereas the decomposition of the

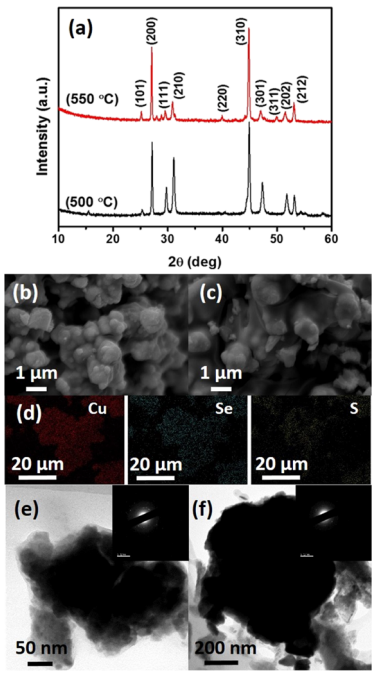

Figure 8. (a) X-ray diffractograms of copper sulfo-selenide from complex (**5**), at 500 and 550 °C. (b,c) SEM images of copper sulfo-selenide prepared at 500 and 550 °C, respectively. (d) Elemental mapping and (e,f) TEM images of copper sulfo-selenide prepared at 500 and 550 °C, respectively (the inset shows the SAED pattern).

mixed thio-/seleno-complex resulted in the formation of the Cu_3Se_2 phase at both temperatures. As seen for the other samples, the solvent-less decomposition resulted in the formation of particles with agglomerated and randomly oriented sheetlike structures. The morphological analysis of sulfur-incorporated Cu_3Se_2 by SEM (Figure 8b,c) and TEM (Figure 8e,f), at both temperatures, showed the formation of nonuniform and polydispersed sheetlike structures.

The formation of mixed chalcogenide alloys is interesting as earlier reports indicated unsuccessful attempts of alloy formation via the use of a mixed thio-/seleno-complex. For instance, O'Brien and co-workers prepared such mixed anionic complexes of nickel, that is, $Ni[\{(SP^iPr_2)(SeP^iPr_2)N\}_2]$ and $Ni[\{(SeP^iPr_2)(TeP^iPr_2)N\}_2]$ for the preparation of NiSSe or NiSeTe.[54,63] However, the CVD of $Ni[\{(SP^iPr_2)(SeP^iPr_2)N\}_2]$ precursor yielded nickel phosphide or nickel selenide thin films depending on the deposition conditions, whereas $Ni[\{(SeP^iPr_2)(TeP^iPr_2)N\}_2]$ yielded only nickel telluride films. Similarly, the decomposition of $[Ag(^iPr_2P(S)NP(Se)^iPr_2)]_3$ precursors for the deposition of $Ag_2S_{0.5}Se_{0.5}$ thin films via AACVD and LPCVD was not successful.[64c] It was presumed from their study that the final product was formed with the heavier chalcogen atom. However, the solvent-less decomposition shows that the synthetic route plays an important role in determining the nature of the final product.

CONCLUSIONS

Dichalcogenoimidodiphosphinate complexes of Mn and Cu have been synthesized through metathetical reactions. The complexes were employed as single-source precursors to deposit crystalline metal chalcogenides through solvent-less thermolysis. Tuning the structural composition of volatile dichalcogenoimidodiphosphinate molecular precursors may yield manganese and copper sulfides, selenides, or mixed

https://doi.org/10.1021/acs.inorgchem.2c00460
Inorg. Chem. 2022, 61, 6612–6623

sulfo-selenide alloys, by a solvent-less pyrolysis route. It showed that in addition to the nature of the precursor, the synthetic route played a significant role on the phase and composition of the synthesized product. The X-ray single-crystal structure analysis indicated triclinic crystal systems for $[Mn\{(SeP^iPr_2)_2N\}_2]$ **1** and $[Mn\{(SP^iPr_2)(SeP^iPr_2)N\}_2]$ **2**. The decomposition of these molecular precursors yielded materials with sheetlike structures, however, there was no control over size and shape. Moreover, phosphorus appeared as an impurity in the final product. The percentage of phosphorus varied between 4 and 12% for different precursors at different temperatures. Phosphorus contamination was also reported previously for metal chalcogenide thin films deposited from similar ligands and was observed for other phosphorus-based ligands as well, such as chalcogenophosphinates and chalcogenophosphates complexes. The future work on these materials will include molecular structure tuning to investigate the effect of aryl groups or longer alkyl chains on the size and shape of deposited materials. Moreover, different synthetic routes will be tested to see whether they are suitable for the deposition of alloyed films without the incorporation of phosphorus.

■ ASSOCIATED CONTENT

Supporting Information

The Supporting Information is available free of charge at https://pubs.acs.org/doi/10.1021/acs.inorgchem.2c00460.

TGA, p-XRD, SEM, TEM, and EDX images; crystallographic data (excluding structure factors) have been deposited with the Cambridge Crystallographic Data Centre as supplementary publication CCDC-2069431 for **1**, CCDC-2069432 for **2**, and CCDC-2069433 for **HL3**. Copies of the data can be obtained free of charge on application to CCDC, 12 Union Road, Cambridge CB2 1EZ, UK [E-mail: deposit@ccdc.cam.ac.uk] (PDF)

Accession Codes

CCDC 2069431−2069433 contain the supplementary crystallographic data for this paper. These data can be obtained free of charge via www.ccdc.cam.ac.uk/data_request/cif, or by emailing data_request@ccdc.cam.ac.uk, or by contacting The Cambridge Crystallographic Data Centre, 12 Union Road, Cambridge CB2 1EZ, UK; fax: +44 1223 336033.

■ AUTHOR INFORMATION

Corresponding Authors

Temidayo Oyetunde − *Centre for Chemical and Biochemical Research (CCBR), Redeemer's University, Ede, Osun State 232102, Nigeria; Institut für Anorganische und Analytische Chemie, Friedrich-Schiller-Universität Jena, Jena D-07743, Germany;* orcid.org/0000-0003-4582-396X; Email: oyetundetemi@run.edu.ng

Neerish Revaprasadu − *Chemistry Department, University of Zululand, KwaDlangezwa 3886, South Africa;* orcid.org/0000-0001-5730-1232; Email: RevaprasaduN@unizulu.ac.za

Authors

Siphamandla Masikane − *Chemistry Department, University of Zululand, KwaDlangezwa 3886, South Africa*

Malik Dilshad Khan − *Chemistry Department, University of Zululand, KwaDlangezwa 3886, South Africa; Institute of Physical Chemistry, Polish Academy of Sciences, Warsaw 01-224, Poland*

Matthew P. Akerman − *School of Chemistry and Physics, University of KwaZulu-Natal, Pietermaritzburg 3201, South Africa;* orcid.org/0000-0001-5116-488X

Helmar Görls − *Institut für Anorganische und Analytische Chemie, Friedrich-Schiller-Universität Jena, Jena D-07743, Germany*

Winfried Plass − *Institut für Anorganische und Analytische Chemie, Friedrich-Schiller-Universität Jena, Jena D-07743, Germany;* orcid.org/0000-0003-3473-9682

Complete contact information is available at: https://pubs.acs.org/10.1021/acs.inorgchem.2c00460

Notes

The authors declare no competing financial interest.

■ ACKNOWLEDGMENTS

T.O. gratefully acknowledges the scholarship from Deutscher Akademischer Austauschdienst (DAAD) with the number: 57378441 for this research project. The authors would like to acknowledge the MS platform at the Friedrich Schiller University Jena for support in mass spectrometry. W.P. acknowledges the financial support of the Deutsche Forschungsgemeinschaft (PL 155/20-1). N.R. is grateful to the National Research Foundation (NRF) South African Research Chairs Initiative (SARChI) for financial support.

■ REFERENCES

(1) Manivannan, R.; Victoria, S. N. Preparation of chalcogenide thin films using electrodeposition method for solar cell applications − A review. *Sol. Energy* **2018**, *173*, 1144−1157.

(2) Da Silva, R.; Barbosa, R.; Mançano, R. R.; Durães, N.; Pontes, R. B.; Miwa, R. H.; Fazzio, A.; Padilha, J. E. Metal Chalcogenides Janus Monolayers for Efficient Hydrogen Generation by Photocatalytic Water Splitting. *ACS Appl. Nano. Mater.* **2019**, *2*, 890−897.

(3) Barik, R.; Ingole, P. P. Challenges and prospects of metal sulfide materials for supercapacitors. *Curr. Opin. Electrochem.* **2020**, *21*, 327−334.

(4) Gago, A. S.; Luo, Y.; Alonso-Vante, N. Chalcogenide electrocatalysts for energy conversion fuel cell. In *Encyclopaedia of Interfacial Chemistry*; Wandelt, K., Ed.; Elsevier: Oxford, 2018; pp 419−445.

(5) Roychowdhury, S.; Samanta, M.; Banik, A.; Biswas, K. Thermoelectric energy conversion and topological materials based on heavy metal chalcogenides. *J. Sol. State Chem.* **2019**, *275*, 103−123.

(6) Chen, S.; Chen, Z.-J.; Ren, W.; Ai, H.-W. Reaction-Based Genetically Encoded Fluorescent Hydrogen Sulfide Sensors. *J. Am. Chem. Soc.* **2012**, *134*, 9589−9592.

(7) Matthews, P. D.; McNaughter, P. D.; Lewis, D. J.; O'Brien, P. Shining a light on transition metal chalcogenides for sustainable photovoltaics. *Chem. Sci.* **2017**, *8*, 4177−4187.

(8) Tedstone, A. A.; Lewis, D. J.; O'Brien, P. Synthesis, Properties, and Applications of Transition Metal-Doped Layered Transition Metal Dichalcogenides. *Chem. Mater.* **2016**, *28*, 1965−1974.

(9) Mateker, W. R.; McGehee, M. D. Progress in Understanding Degradation Mechanisms and Improving Stability in Organic Photovoltaics. *Adv. Mater.* **2017**, *29*, No. 1603940.

(10) Woods-Robinson, R.; Han, Y.; Zhang, H.; Ablekim, T.; Khan, I.; Persson, K. A.; Zakutayev, A. Wide Band Gap Chalcogenide Semiconductors. *Chem. Rev.* **2020**, *120*, 4007−4055.

(11) Li, Y.-Y.; Wang, W.-J.; Wang, H.; Lin, H.; Wu, L.-M. Mixed-anion inorganic compounds: A favorable candidate for infrared nonlinear optical materials. *Cryst. Growth Des.* **2019**, *19*, 4172−4192.

(12) Gao, W.; Li, Y.; Guo, J.; Ni, M.; Liao, M.; Mo, H.; Li, J. Narrow-gap physical vapour deposition synthesis of ultrathin SnS 1−

x Se x (0≤ x≤ 1) two-dimensional alloys with unique polarized Raman spectra and high (opto) electronic properties. *Nanoscale* **2018**, *10*, 8787−8795.
(13) Khan, M. D.; Awan, S. U.; Zequine, C.; Zhang, C.; Gupta, R. K.; Revaprasadu, N. Controlled synthesis of Sb2 (S1−x Se x) 3 (0≤ x≤ 1) solid solution and the effect of composition variation on electrocatalytic energy conversion and storage. *ACS Appl. Energy Mater.* **2020**, *3*, 1448−1460.
(14) Khan, M. D.; Aamir, M.; Murtaza, G.; Malik, M. A.; Revaprasadu, N. Structural investigations of SnS 1− x Se x solid solution synthesized from chalcogeno-carboxylate complexes of organo-tin by colloidal and solvent-less routes. *Dalton Trans.* **2018**, *47*, 10025−10034.
(15) Khan, M. D.; Opallo, M.; Revaprasadu, N. Colloidal synthesis of metal chalcogenide nanomaterials from metal−organic precursors and capping ligand effect on electrocatalytic performance: progress, challenges and future perspectives. *Dalton Trans.* **2021**, *50*, 11347−11359.
(16) Khan, M. D.; Malik, M. A.; Revaprasadu, N. Progress in selenium based metal-organic precursors for main group and transition metal selenide thin films and nanomaterials. *Coord. Chem. Rev.* **2019**, *388*, 24−47.
(17) (a) Lathe, A.; Palve, A. M. Reduced graphene oxide-decorated CdS/ZnO nanocomposites for photo-reduction of hexavalent chromium and photo-degradation of methylene blue. *Dalton Trans.* **2021**, *50*, 14163−14175. (b) Palve, A. M.; Joshi, P. V.; Puranik, V.; Garje, S. S. Synthesis and X-ray single crystal structure of a cadmium(II) acetophenone thiosemicarbazone complex and its use as a single-source precursor for the preparation of CdS nanocrystallites and thin films. *Polyhedron* **2013**, *61*, 195−201. (c) Shombe, G. B.; Razzaque, S.; Khan, M. D.; Nyokong, T.; Mashazi, P.; Choi, J.; Bhoyate, S.; Gupta, R. K.; Revaprasadu, N. Low temperature scalable synthetic approach enabling high bifunctional electrocatalytic performance of $NiCo_2S_4$ and $CuCo_2S_4$ thiospinels. *RSC Adv.* **2021**, *11*, 31533−31546. (d) Tigwere, G. A.; Khan, M. D.; Nyamen, L. D.; Aboud, A. A.; Moyo, T.; Dlamini, S. T.; Ndifon, P. T.; Revaprasadu, N. Molecular precursor route for the phase selective synthesis of α-MnS or metastable γ-MnS nanomaterials for magnetic studies and deposition of thin films by AACVD. *Mater. Sci. Semicond. Process.* **2022**, *139*, No. 106330. (e) Ketchemen, K. I. Y.; Khan, M. D.; Mlowe, S.; Akerman, M. P.; Vitorica-Yrezabal, I.; Whitehead, G.; Nyamen, L. D.; Ndifon, P. T.; Revaprasadu, N.; O'Brien, P. Crystal structures and physicochemical studies of some novel divalent and trivalent transition metal chelates of *N*-morpholine-*N*′-benzoylthiourea. *J. Mol. Struct.* **2021**, *12229*, No. 129791.
(18) (a) Oyetunde, T.; Afzaal, M.; Vincent, M. A.; O'Brien, P. The deposition of cadmium selenide and cadmium phosphide thin films from cadmium thioselenoimidodiphosphinate by AACVD and the formation of an aromatic species. *Dalton Trans.* **2019**, *48*, 1436−1442. (b) Oyetunde, T.; Afzaal, M.; Vincent, M. A.; O'Brien, P. Aerosol-assisted CVD of cadmium diselenoimidodiphosphinate and formation of a new $^{i}Pr_2N_2P_3^+$ ion supported by combined DFT and mass spectrometric studies. *Dalton Trans.* **2016**, *45*, 18603−18609. (c) Oyetunde, D.; Afzaal, M.; Vincent, M. A.; Hillier, I. H.; O'Brien, P. Cadmium Sulfide and Cadmium Phosphide Thin Films from a Single Cadmium Compound. *Inorg. Chem.* **2011**, *50*, 2052−2054.
(19) Oyetunde, T.; Afzaal, M.; O'Brien, P. Phenyl substituted ditelluro-imidodiphosphinate complexes of iron, nickel, palladium and platinum, and their pyrolysis studies generating metal tellurides. *Polyhedron* **2019**, *160*, 157−162.
(20) Oyetunde, T.; Omorogie, M. O.; O'Brien, P. Ferromagnetic $FeSe_2$ from a mixed sulfur-selenium complex of iron [Fe-$\{(SePPh_2NPPh_2S)_2N\}_3$] through pyrolysis. *Heliyon* **2020**, *6*, No. e03763.
(21) Panneerselvam, A.; Nguyen, C. Q.; Waters, J.; Malik, M. A.; O'Brien, P.; Raftery, J.; Helliwell, M. Ligand influence on the formation of P/Se semiconductor materials from metal−organic complexes. *Dalton Trans.* **2008**, 4499−4506.
(22) Copsey, M. C.; Panneerselvam, A.; Afzaal, M.; Chivers, T.; O'Brien, P. Syntheses, X-ray structures and AACVD studies of group 11 ditelluroimidodiphosphinate complexes. *Dalton Trans.* **2007**, 1528−1538.
(23) Lewis, E.; Haigh, S.; O'Brien, P. The synthesis of metallic and semiconducting nanoparticles from reactive melts of precursors. *J. Mater. Chem. A* **2014**, *2*, 570−580.
(24) Shombe, G. B.; Khan, M. D.; Zequine, C.; Zhao, C.; Gupta, R. K.; Revaprasadu, N. Direct solvent free synthesis of bare α-NiS, β-NiS and α-β-NiS composite as excellent electrocatalysts: Effect of self-capping on supercapacitance and overall water splitting activity. *Sci. Rep.* **2020**, *10*, 3260.
(25) Monsef, R.; Maryam, G.-A.; Masoud, S.-N. Design of Magnetically Recyclable Ternary $Fe_2O_3/EuVO_4/g\text{-}C_3N_4$ Nanocomposites for Photocatalytic and Electrochemical Hydrogen Storage. *ACS Appl. Energy Mater.* **2021**, *4*, 680−695.
(26) Jafari, M.; Sobhani, A.; Masoud, S.-N. Effect of preparation conditions on synthesis of Ag_2Se nanoparticles by simple sonochemical method assisted by thiourea. *J. Ind. Eng. Chem.* **2014**, *20*, 3775−3779.
(27) Sahar, Z.-A.; Sobhan, M.-D.; Masoud, S.-N. Nd_2O_3-SiO_2 nanocomposites: A simple sonochemical preparation, characterization and photocatalytic activity. *Ultrason. Sonochem.* **2018**, *42*, 171−182.
(28) Sobhan, M.; Sahar, Z.-A.; Masoud, S.-N. Novel simple solvent-less preparation, characterization and degradation of the cationic dye over holmium oxide ceramic nanostructures. *Ceram. Int.* **2015**, *41*, 9593−9601.
(29) Masoud, S.-N.; Davar, F.; Mazaheri, M. Synthesis of Mn_3O_4 nanoparticles by thermal decomposition of a [bis(salicylidiminato)-manganese(II)] complex. *Polyhedron* **2008**, *27*, 3467−3471.
(30) Shahla, A.-F.-F.; Ghanbari, D.; Masoud, S.-N. Photoluminescence carbon dot as a sensor for detecting of *Pseudomonas aeruginosa* bacteria: Hydrothermal synthesis of magnetic hollow $NiFe_2O_4$-carbon dots nanocomposite material. *Composites, Part B* **2019**, *161*, 564−577.
(31) Motahari, F.; Mozdianfard, M. R.; Masoud, S.-N. Synthesis and adsorption studies of NiO nanoparticles in presence of H_2acacen ligand, for removing Rhodamine B in wastewater treatment. *Process Saf. Environ. Prot.* **2015**, *93*, 282−292.
(32) Amiri, M.; Masoud, S.-N.; Pardakhty, A.; Ahmadi, M.; Akbari, A. Caffeine: A novel green precursor for synthesis of magnetic $CoFe_2O_4$ nanoparticles and pH-sensitive magnetic alginate beads for drug delivery. *Mater. Sci. Eng., C* **2017**, *76*, 1085−1093.
(33) Fini, S. A.-F.; Ghanbari, D.; Amiri, O.; Masoud, S.-N. Electrospinning of cellulose acetate nanofibers/Fe/carbon dot as photoluminescence sensor for mercury (II) and lead (II) ions. *Carbohydr. Polym.* **2020**, *229*, No. 115428.
(34) Sahar, Z.-A.; Morassaei, M. S.; Amiri, O.; Masoud, S.-N.; Foong, L. K. $Nd_2Sn_2O_7$ nanostructures: Green synthesis and characterization using date palm extract, a potential electrochemical hydrogen storage material. *Ceram. Int.* **2020**, *46*, 17186−17196.
(35) Javed, M. S.; Shah, S. S. A.; Hussain, S.; Tan, S.; Mai, W. Mesoporous manganese-selenide microflowers with enhanced electrochemical performance as a flexible symmetric 1.8 V supercapacitor. *Chem. Eng. J.* **2020**, *382*, No. 122814.
(36) Qiao, F.; Chen, L.; Li, X.; Li, L.; Ai, S. Peroxidase-like activity of manganese selenide nanoparticles and its analytical application for visual detection of hydrogen peroxide and glucose. *Sens. Actuators, B* **2014**, *193*, 255−262.
(37) Sobhani, A.; Salavati-Niasari, M. Transition metal selenides and diselenides: Hydrothermal fabrication, investigation of morphology, particle size and their applications in photocatalyst. *Adv. Colloid Interface Sci.* **2021**, *287*, No. 102321.
(38) Kucharek, J.; Bozek, R.; Pacuski, W. MnSe—Molecular Beam Epitaxy Growth and Optical Characterisation. *Acta Phys. Pol., A* **2019**, *136*, 598−602.
(39) Raman, V.; Chinnadurai, D.; Rajmohan, R.; Chebrolu, V. T.; Rajangam, V.; Kim, H.-J. Transition metal chalcogenide based MnSe heterostructured with $NiCo_2O_4$ as a new high performance electrode

https://doi.org/10.1021/acs.inorgchem.2c00460
Inorg. Chem. 2022, 61, 6612−6623

material for capacitive energy storage. *New J. Chem.* **2019**, *43*, 12630−12640.
(40) (a) Orletsky, I. G.; Ilashchuk, M. I.; Maistruk, E. V.; Parkhomenko, H. P.; Marianchuk, P. D.; Koziarskyi, I. P.; Koziarskyi, D. P. Electrical properties of heterostructures MnS/nCdZnTe obtained by spray pyrolysis. *Mater. Res. Express* **2021**, *8*, No. 015905. (b) Hannachi, A.; Segura, A.; Maghraoui-Meherzi, H. Growth of manganese sulfide (α-MnS) thin films by thermal vacuum evaporation: Structural, morphological and optical properties. *Mater. Res. Express* **2016**, *181*, 326−332.
(41) Hou, X.; Xie, P.; Xue, S.; Feng, H.; Li, L.; Liu, Z.; Zou, R. The study of morphology-controlled synthesis and the optical properties of CuSe nanoplates based on the hydrothermal method. *Mater. Sci. Semicond. Process.* **2018**, *79*, 92−98.
(42) Sudha, A. P.; Henry, J.; Mohanraj, K.; Sivakumar, G. Effect of Na doping on structural, optical, and electrical properties of Cu_2Se thin films prepared by chemical bath deposition method. *Appl. Phys. A: Mater. Sci. Process.* **2018**, *124*, 164.
(43) Yang, C.-T.; Hsiang, H.-I. Rapid synthesis and characterization of nearly dispersed marcasite $CuSe_2$ and berzelianite Cu_2Se crystallites using the chemical reduction process. *Mater. Res. Bull.* **2018**, *97*, 30−36.
(44) Chen, X.; Yang, J.; Wu, T.; Li, L.; Luo, W.; Jianga, W.; Wang, L. Nanostructured binary copper chalcogenides: synthesis strategies and common applications. *Nanoscale* **2018**, *10*, 15130−15163.
(45) (a) Cupertino, D.; Birdsall, D. J.; Slawin, A. M. Z.; Woollins, J. D. The preparation and coordination chemistry of $^{i}Pr_2P(E)NHP(E')^{i}Pr_2$ (E, E′=Se; E=Se, E′=S; E=S, E′=O; E,E′=O. *Inorg. Chim. Acta* **1999**, *290*, 1−7. (b) Cupertino, D.; Kyete, R.; Slawin, A. M. Z.; Williams, D. J.; Woollins, J. D. Preparation and Single-Crystal Characterization of $^{i}Pr_2P(S)NHP(S)^{i}Pr_2$ and Homoleptic $[^{i}Pr_2P(S)NP(S)^{i}Pr_2]^-$ Complexes of Zinc, Cadmium, and Nickel. *Inorg. Chem.* **1996**, *35*, 2695−2697. (c) Maganas, D.; Staniland, S. S.; Grigoropoulos, A.; White, F.; Parsons, S.; Robertson, N.; Kyritsis, P.; Pneumatikakis, G. Structural, spectroscopic and magnetic properties of $M[R_2P(E)NP(E)R'_2]_2$ complexes, M = Co, Mn, E = S, Se and R, R' = Ph or ^{i}Pr. Covalency of M−S bonds from experimental data and theoretical calculations. *Dalton Trans.* **2006**, 2301−2315.
(46) Nonius, B. V. *COLLECT, Data Collection Software*; Netherlands; 1998.
(47) Otwinowski, Z.; Minor, W. Processing of X-Ray Diffraction Data Collected in Oscillation Mode. In *Methods in Enzymology, Macromolecular Crystallography, Part A*; Carter, C. W., Sweet, R. M., Eds.; Academic Press: Cambridge, MA, 1997; Vol. *276*, pp 307−326
(48) Krause, L.; Herbst-Irmer, R.; Sheldrick, G. M.; Stalke, D. Comparison of silver and molybdenum microfocus X-ray sources for single-crystal structure determination. *J. Appl. Crystallogr.* **2015**, *48*, 3−10.
(49) Sheldrick, G. M. A short history of SHELX. *Acta Crystallogr., Sect. A: Found. Crystallogr.* **2008**, *64*, 112−122.
(50) Macrae, C. F.; Sovago, I.; Cottrell, S. J.; Galek, P. T. A.; McCabe, P.; Pidcock, E.; Platings, M.; Shields, G. P.; Stevens, J. S.; Towler, M.; Wood, P. A. Mercury 4.0: from visualization to analysis, design and prediction. *J. Appl. Crystallogr.* **2020**, *53*, 226−235.
(51) Cupertino, D. C.; Keyte, R. W.; Slawin, A. M. Z.; Woollins, J. D. Synthesis and coordination chemistry of tetrabutyldithioimidodiphosphinates. *Polyhedron* **1999**, *18*, 707−716.
(52) Craig, N. C.; Chen, A.; Suh, K. H.; Klee, S.; Melau, G. C.; Winnewisser, B. P.; Winnewisser, M. Contribution to the Study of the Gauche Effect. The Complete Structure of the Anti Rotamer of 1, 2-Difluoroethane. *J. Am. Chem. Soc.* **1997**, *119*, 4789−4790.
(53) Boadi, N. O.; Saah, S. A.; Raftery, J.; Awudza, J. A. M. Hot-Injection Synthesis of PbE (E = S, Se) Nanoparticles from Dichalcogenoimidophosphinato Lead (II) Complexes. *ChemistrySelect* **2019**, *4*, 13908−13911.
(54) Panneerselvam, A.; Malik, M. A.; Afzaal, M.; O'Brien, P.; Helliwell, M. The chemical vapor deposition of nickel phosphide or selenide thin films from a single precursor. The Chemical Vapor Deposition of Nickel Phosphide or Selenide Thin Films from a Single Precursor. *J. Am. Chem. Soc.* **2008**, *130*, 2420−2421.
(55) Mónica, M.-C.; Raymundo, C.-O.; Jocelyn, A.-G.; Toscano, R. A.; Jancik, V.; Verónica, G.-M.; Simón, H.-O. Synthesis and structural characterization of gallium and indium complexes obtained from redistribution reactions of mixed chalcogen-imidodiphosphinate ligands. *J. Org. Chem.* **2005**, *690*, 3054−3060.
(56) Crouch, D. J.; Hatton, P. M.; Helliwell, M.; O'Brien, P.; Raftery, J. Organomercury-based imino-bis(diisopropylphosphine chalcogenide) complexes: synthesis and characterisation of novel hybrid "single-source precursors" for mercury chalcogenide solid-state materials. *Dalton Trans.* **2003**, 2761−2766.
(57) Raymundo, C.-O.; Mónica, M.-C.; Verónica, G.-M.; Rafael, C.-B.; Rubén, A. T.; Simón, H.-O. True square planar $[M\{N(SeP^{i}Pr_2)_2\text{-}Se,Se'\}_2]$ [M = Sn, Se] complexes. An extraordinary geometrical arrangement for well known centers [Sn(II), Se(II)]. *Dalton Trans.* , *2005*, 1017, 1018, DOI: 10.1039/B418198K.
(58) Ritch, J. S.; Chivers, T.; Ahmad, K.; Afzaal, M.; O'Brien, P. Synthesis, Structures, and Multinuclear NMR Spectra of Tin(II) and Lead(II) Complexes of Tellurium-Containing Imidodiphosphinate Ligands: Preparation of Two Morphologies of Phase-Pure PbTe from a Single-Source Precursor. *Inorg. Chem.* **2010**, *49*, 1198.
(59) Gilby, L. M.; Piggott, B. The synthesis and X-ray structure of cobalt(II) complexes of iminobis(phosphinechalcogenides), $[Co\{N(XPR_2)_2\text{−}X,X'\}_2]$ (X=S or Se; R=Ph or ^{i}Pr). *Polyhedron* **1999**, *18*, 1077−1082.
(60) Frisch, M. J.; Trucks, G. W.; Schlegel, H. B.; Scuseria, G. E.; Robb, M. A.; Cheeseman, J. R.; Scalmani, G.; Barone, V.; Mennucci, B.; Petersson, G. A.; Nakatsuji, H.; Caricato, M.; Li, X.; Hratchian, H. P.; Izmaylov, A. F.; Bloino, J.; Zheng, G.; Sonnenberg, J. L.; Hada, M.; Ehara, M.; Toyota, K.; Fukuda, R.; Hasegawa, J.; Ishida, M.; Nakajima, T.; Honda, Y.; Kitao, O.; Nakai, H.; Vreven, T.; Montgomery, J. A., Jr.; Peralta, J. E.; Ogliaro, F.; Bearpark, M.; Heyd, J. J.; Brothers, E.; Kudin, K. N.; Staroverov, V. N.; Kobayashi, R.; Normand, J.; Raghavachari, K.; Rendell, A.; Burant, J. C.; Iyengar, S. S.; Tomasi, J.; Cossi, M.; Rega, N.; Millam, J. M.; Klene, M.; Knox, J. E.; Cross, J. B.; Bakken, V.; Adamo, C.; Jaramillo, J.; Gomperts, R.; Stratmann, R. E.; Yazyev, O.; Austin, A. J.; Cammi, R.; Pomelli, C.; Ochterski, J. W.; Martin, R. L.; Morokuma, K.; Zakrzewski, V. G.; Voth, G. A.; Salvador, P.; Dannenberg, J. J.; Dapprich, S.; Daniels, A. D.; Farkas, O.; Foresman, J. B.; Ortiz, J. V.; Cioslowski, J.; Fox, D. J. *Gaussian 09, Revision E.01*; Gaussian, Inc.: Wallingford, CT, 2009.
(61) Dennington, R. D.; Keith, T.; Millam, J. M. *GaussView, Version 5;* Semichem Inc.: Shawnee Mission, KS, 2009.
(62) Waters, J.; Crouch, D.; Raftery, J.; O'Brien, P. Deposition of bismuth chalcogenide thin films using novel single-source precursors by metal-organic chemical vapor deposition. *Chem. Mater.* **2004**, *16*, 3289−3298.
(63) Robertson, S. D.; Chivers, T.; Akhtar, J.; Afzaal, M.; O'Brien, P. Nickel (II) complexes of heterodichalcogenido and monochalcogenido imidodiphosphinate ligands: AACVD synthesis of nickel ditelluride. *Dalton Trans.* **2008**, 7004−7011.
(64) (a) Afzaal, M.; Crouch, D.; Malik, M. A.; Motevalli, M.; O'Brien, P.; Park, J.-H.; Woollins, J. D. Deposition of II-VI Thin Films by LP-MOCVD Using Novel Single-Source Precursors. *Eur. J. Inorg. Chem.* **2004**, 171−177. (b) Afzaal, M.; Crouch, D.; O'Brien, P.; Park, J.-H. Metal-organic chemical vapour deposition of β-In_2S_3 thin films using a single-source precursor. *J. Mater. Sci.: Mater. Electron.* **2003**, *14*, 555−557. (c) Panneerselvam, A.; Nguyen, C. Q.; Malik, M. A.; O'Brien, P.; Raftery, J. The CVD of silver selenide films from dichalcogenophosphinato and imidodichalcogenodiphosphinatosilver-(I) single-source precursors. *J. Mater. Chem.* **2009**, *19*, 419−427.

https://doi.org/10.1021/acs.inorgchem.2c00460
Inorg. Chem. 2022, 61, 6612−6623